

Orbital climate variability on the northeastern Tibetan Plateau across the Eocene–Oligocene transition

Hong Ao ^{1,2,3,4}✉, Guillaume Dupont-Nivet ^{5,6,7}✉, Eelco J. Rohling ^{8,9}, Peng Zhang ^{1,3}, Jean-Baptiste Ladant ¹⁰, Andrew P. Roberts ⁸, Alexis Licht ¹¹, Qingsong Liu¹², Zhonghui Liu ¹³, Mark J. Dekkers ¹⁴, Helen K. Coxall ¹⁵, Zhangdong Jin ^{1,2,16}, Chunju Huang ⁴, Guoqiao Xiao ⁴, Christopher J. Poulsen ¹⁰, Natasha Barbolini ¹⁷, Niels Meijer ⁷, Qiang Sun ¹⁸, Xiaoke Qiang ¹, Jiao Yao ¹ & Zhisheng An ^{1,2,19}✉

The first major build-up of Antarctic glaciation occurred in two consecutive stages across the Eocene–Oligocene transition (EOT): the EOT-1 cooling event at ~34.1–33.9 Ma and the Oi-1 glaciation event at ~33.8–33.6 Ma. Detailed orbital-scale terrestrial environmental responses to these events remain poorly known. Here we present magnetic and geochemical climate records from the northeastern Tibetan Plateau margin that are dated precisely from ~35.5 to 31 Ma by combined magneto- and astro-chronology. These records suggest a hydroclimate transition at ~33.7 Ma from eccentricity dominated cycles to oscillations paced by a combination of eccentricity, obliquity, and precession, and confirm that major Asian aridification and cooling occurred at Oi-1. We conclude that this terrestrial orbital response transition coincided with a similar transition in the marine benthic $\delta^{18}\text{O}$ record for global ice volume and deep-sea temperature variations. The dramatic reorganization of the Asian climate system coincident with Oi-1 was, thus, a response to coeval atmospheric CO_2 decline and continental-scale Antarctic glaciation.

¹State Key Laboratory of Loess and Quaternary Geology, Institute of Earth Environment, Chinese Academy of Sciences, Xi'an, China. ²CAS Center for Excellence in Quaternary Science and Global Change, Chinese Academy of Sciences, Xi'an, China. ³Open Studio for Oceanic-Continental Climate and Environment Changes, Pilot National Laboratory for Marine Science and Technology (Qingdao), Qingdao, China. ⁴State Key Laboratory of Biogeology and Environmental Geology, School of Earth Sciences, China University of Geosciences, Wuhan, China. ⁵Université de Rennes, CNRS, Géosciences Rennes, UMR, 6118 Rennes, France. ⁶Key Laboratory of Orogenic Belts and Crustal Evolution, Peking University, Beijing, China. ⁷Universität Potsdam, Institute of Geosciences, Potsdam, Germany. ⁸Research School of Earth Sciences, Australian National University, Canberra, Australia. ⁹Ocean and Earth Science, University of Southampton, National Oceanography Centre, Southampton, UK. ¹⁰Department of Earth and Environmental Sciences, University of Michigan, Ann Arbor, MI, USA. ¹¹Department of Earth and Space Sciences, University of Washington, Seattle, USA. ¹²Centre for Marine Magnetism (CM2), Department of Ocean Science and Engineering, Southern University of Science and Technology, Shenzhen, China. ¹³Department of Earth Sciences, University of Hong Kong, Hong Kong, China. ¹⁴Paleomagnetic Laboratory 'Fort Hoofddijk', Department of Earth Sciences, Faculty of Geosciences, Utrecht University, Utrecht, The Netherlands. ¹⁵Department of Geological Sciences, Stockholm University, Stockholm, Sweden. ¹⁶Institute of Global Environmental Change, Xi'an Jiaotong University, Xi'an, China. ¹⁷Department of Ecosystem and Landscape Dynamics, Institute for Biodiversity and Ecosystem Dynamics, University of Amsterdam, Amsterdam, The Netherlands. ¹⁸College of Geology and Environment, Xi'an University of Science and Technology, Xi'an, China. ¹⁹Interdisciplinary Research Center of Earth Science Frontier, Beijing Normal University, Beijing, China. ✉email: aohong@ieecas.cn; guillaume.dupont-nivet@univ-rennes1.fr; anzs@loess.llqg.ac.cn

The Eocene–Oligocene transition (EOT) at ~34 Ma marks the main transition from the early Cenozoic greenhouse to the modern icehouse world¹. Marine records and climate model experiments suggest that this key transition occurred in two stages^{2–5}. The first stage (EOT-1) at ~34.1–33.9 Ma, in the upper portion of the reversed polarity chron C13r, is marked by moderate cooling and modest Antarctic ice volume increase^{2–5}. The second, more dramatic, stage (Oi-1 glaciation) occurred around the C13r–C13n boundary at ~33.8–33.6 Ma and represents the culmination of the greenhouse-to-icehouse transition with ice-sheet expansion to the Antarctic coastline^{2–5}. Oceanic and atmospheric circulation, ocean productivity, ocean carbonate compensation depth, and the global carbon cycle changed substantially from the late Eocene to early Oligocene^{3–12}. Detailed reconstructions of climate variability across the EOT in the oceanic and continental realms, and in both the northern and southern hemispheres, help to elucidate the dynamics and interactions of large-scale climate changes in response to atmospheric CO₂ decrease and global cooling^{3,6,9,13–15}.

Terrestrial EOT records are relatively rare and include a few from East Asia (Maoming, Xining, Qaidam, and Junggar basins, and Mongolia)^{9,14,16–23}, central North America^{13,24}, southernmost South America²⁵, and Northern Europe²⁶ (Supplementary Fig. 1). These terrestrial records reveal long-term changes across the EOT, including a broad shift to cooler and drier continental climate that is generally consistent with ocean cooling^{15,27–29}. However, they often lack sufficient temporal resolution to constrain associated short-term climate events and orbital-scale changes. As a result, the timing of the major terrestrial climate shift, and its relationship with the marine EOT-1 and Oi-1 events, remains uncertain. Continuous and expanded (>500 m thick) Eocene to Oligocene playa-palaeolake sequences on the NE Tibetan Plateau margin, including those in the Lanzhou and Xining basins (Fig. 1), allow high-resolution analysis of Tibetan EOT sequences. The EOT has been pinpointed stratigraphically in the Xining Basin, and has been associated with terrestrial cooling and aridification based on environmental magnetic, clay mineral, isotopic, palaeontological, and sedimentological changes^{9,14,16–18}. These studies suggest that the terrestrial playa-palaeolake sequences on the NE Tibetan Plateau provide sensitive archives of past climate changes on land and have the potential to reveal details of orbital-scale terrestrial responses to global events through the EOT. At present, analysis of both marine^{15,29} and terrestrial^{9,13,14,16–21,23,25,26} records has focused primarily on general long-term cooling and/or aridification trends across the EOT, but much less on orbital-scale climate variability^{4,9,11,12,16,30–32}, because of a lack of sufficiently high-resolution palaeoclimate records that span continuously from the late Eocene to early Oligocene.

Here, we present environmental magnetic and elemental records for the ~35.5–31 Ma age interval from the Lanzhou Basin, located southeast of the Xining Basin on the NE Tibetan Plateau margin. They suggest an orbital variability shift for terrestrial Asian hydroclimate at ~33.7 Ma and constrain the major Asian aridification and cooling episode to coincide with the Oi-1 event. Based on terrestrial-to-marine correlations, we attribute these terrestrial climate changes to atmospheric CO₂ decline and major Antarctic glaciation at Oi-1.

Results

Setting, stratigraphy, and sedimentology of Eocene–Oligocene sediments in the Lanzhou Basin. The NE Tibetan Plateau, both today and during the EOT, is situated in a transitional semi-arid region under the combined influence of the Asian summer and winter monsoons and the Westerlies, and is, therefore, sensitive to hydroclimate (moisture) changes^{9,10,14} (Fig. 1). In the

Palaeogene, both the Lanzhou and Xining basins were part of the larger Longzhong Basin that resulted from slow subsidence after a Late Cretaceous fault initiation³³. The Lanzhou Basin was later compartmentalized by fault reactivation related to the Indo-Asia collision^{34,35} and is now bounded by the West Qinling mountains (dominated by Palaeozoic sedimentary rocks and Lower Palaeozoic plutonic rocks) in the south and the East Qilian Shan (dominated by Triassic submarine fan deposits and Permo-Triassic plutonic rocks) in the west and north³⁵ (Fig. 1; Supplementary Fig. 2). The Lanzhou Basin presents a relatively small area of roughly 300 km² that is filled with a thick (>1500 m) and mostly continuous sequence of Eocene–Miocene playa-palaeolake sediments that were transported primarily from the surrounding highlands³⁵. Composed mostly of red fine-grained deposits, they provide an important early Eocene to Miocene regional climate archive^{35–38}.

The Duitingou section (36°13'N, 103°37'E; 1,800 m elevation) studied here is located in the center of the Lanzhou Basin (Fig. 1). From older to younger, the Xiliugou, Yehucheng, and Xianshuihe Formations are recognized (Supplementary Fig. 3). The latest Eocene to earliest Oligocene succession studied here (383–570 m stratigraphic level within the Duitingou section) is entirely within the Yehucheng Formation. The lithology comprises mudstone, siltstone, and fine sandstone successions with distinct gypsiferous cyclic intercalations (Supplementary Fig. 3). The overlying Oligocene–Miocene Xianshuihe Formation consists mainly of light red mudstones that are intercalated with sandstone or conglomerate packages^{37,38}, while the underlying early Eocene Xiliugou Formation consists of red massive sandstones (Supplementary Fig. 3).

Cyclic gypsiferous intercalations in the mudstone/siltstone are typical features of the Yehucheng Formation in the Lanzhou Basin (Fig. 2; Supplementary Fig. 3) and are similar to those in the coeval Mahalagou Formation in the nearby Xining Basin, which were modulated by orbital climate oscillations^{9,16,32}. Gypsum beds are white or greyish-green, and vary in thickness between *ca* 0.5 and 4 m. There are two main gypsum facies: (1) gypsum beds that consist of millimetre- to centimetre-scale fine-grained gypsum laminae that are generally associated with variable amounts of reddish-brown/greyish-olive laminated mudstone/siltstone beds, and (2) gypsum beds that are dominated by decimetre- to metre-thick tabular or nodular beds of alabastrine gypsum with rarely preserved lacustrine laminations due to chickenwire structures, displacive enterolithic veins, and cracks. Cyclic gypsiferous intercalations indicate perennial subaqueous playa saline lake conditions with higher groundwater levels that allowed solutes to develop metre-scale gypsum layers^{9,32}. In contrast, mudstone beds are reddish brown to dark red and massive. Notably, their red colour and widespread cm-scale slickensides (Supplementary Fig. 3) suggest that they have been subjected to occasional oxidizing conditions, i.e., a distal alluvial fan environment and ephemeral subaerial exposure with moderate pedogenesis under a low-gradient floodplain or dry distal mudflat environment⁹. The absence of colour mottling, gley-features, and carbonate nodules indicates that the regional palaeoenvironment was not sufficiently humid for intense pedogenesis and soil formation after deposition³². Greyish white siltstones are likely to have been deposited under subaqueous alluvial to shallow playa lake conditions, while light red siltstones possibly formed under alluvial to even shallower ephemeral playa lake conditions with occasional subaerial exposure. Field investigation suggests that both mudstone and siltstone beds are homogeneous throughout this section, without apparent changes from the lower to upper intervals, which is supported by the mean grain size record (Fig. 2). They occasionally have variable small amounts of dispersed fine-grained or lenticular gypsum grains, which may have originated from evaporating

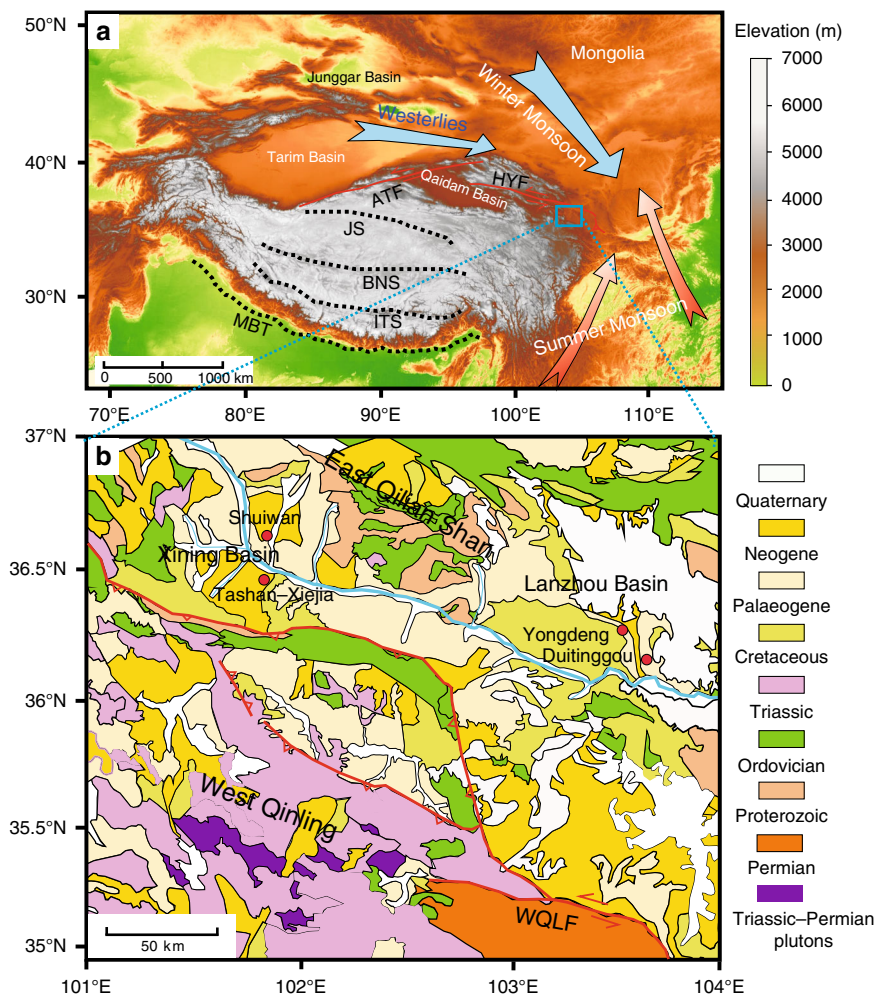


Fig. 1 Site location. **a** Topographic map of the present-day Tibetan Plateau region with relevant atmospheric features (indicated with blue and brown arrows) and major tectonic features (MBT, Main Boundary Thrust of the Himalaya; ITS, Indus-Tsangpo Suture; BNS, Bangong-Nujiang Suture; JS: Jinsha Suture; ATF, Altyn Tagh Fault; HYF, Haiyuan Fault). **b** Simplified geological map of the Lanzhou and Xining basins with the West Qinling Fault (WQLF) and locations of sections (red solid circles) mentioned in the text.

phreatic groundwater, occasional surface waters percolating into the sediment, and/or riverine input of previously formed gypsum grains³². In addition, four 1–3 m thick greyish-white fine sand beds were deposited in the Yehucheng Formation under subaqueous alluvial to shallow playa lake conditions. They have larger mean grain size values than the (gypsiferous) siltstone and mudstone beds (Fig. 2). Potential bioturbational or pedogenic mixing was not significant as suggested by massive mudstones, often laminated gypsum layers, siltstones with clear linear bedding, rare centimetre-scale crossbedding, and absence of root and burrow traces. Similar to comparable deposits in the Xining Basin, we infer that sediment deposition occurred in distal alluvial playa-palaeolake environments: gypsum intervals formed during perennial subaqueous playa saline lake conditions, greyish white or light red siltstone intervals formed during shallow playa lake to alluvial anoxic subaqueous conditions, and red mudstone intervals formed during distal alluvial fan conditions^{9,16,32,39}. The gypsum and siltstone intervals corresponding to perennial anoxic alluvial to playa lake conditions may relate to higher water supply than the mudstone intervals that correspond to oxic distal alluvial fan conditions^{9,16,32,39}. At the 502-m level in the Duitinggou section, a notable absence of gypsum beds indicates a marked environment shift (Fig. 2). In the neighbouring Xining Basin, a similar change occurred during the EOT, and is

interpreted to indicate a groundwater level decrease associated with regional aridification^{9,16,32}.

Late Eocene to early Oligocene magneto-astrochronology from the Lanzhou Basin. Constrained by mammal and pollen biostratigraphy, the Xianshuihe Formation magnetostratigraphy^{37,38} in the Duitinggou section (0–383 m) has been documented to range from polarity chron C5En down to uppermost chron C12r, with ages from ~18 to 31 Ma (Supplementary Fig. 4). This chronology is supported by consistent correlations with biostratigraphic and magnetostratigraphic records from the neighbouring Xining Basin^{34,40} (Supplementary Fig. 4). Combining the established chronology of the concordantly overlying Xianshuihe Formation^{37,38}, detailed palaeomagnetic analysis (Supplementary Note 1; Supplementary Figs. 4–6) provides a downward magnetostratigraphic continuation from polarity chrons C12r to C16n. In for the Yehucheng Formation, with magnetostratigraphic ages of ~31–35.7 Ma according to the 2012 geomagnetic polarity time scale (GPTS)⁴¹ (Fig. 2). Consistent with the Yongdeng section (~40 km northwest of the Duitinggou section) in the northern Lanzhou Basin³⁶, our data suggest that the top of reversed polarity chron C12r falls within a basin-wide yellow sand layer (marker layer A), which contains an early Oligocene mammal fauna and marks the boundary between the Yehucheng and Xianshuihe Formations

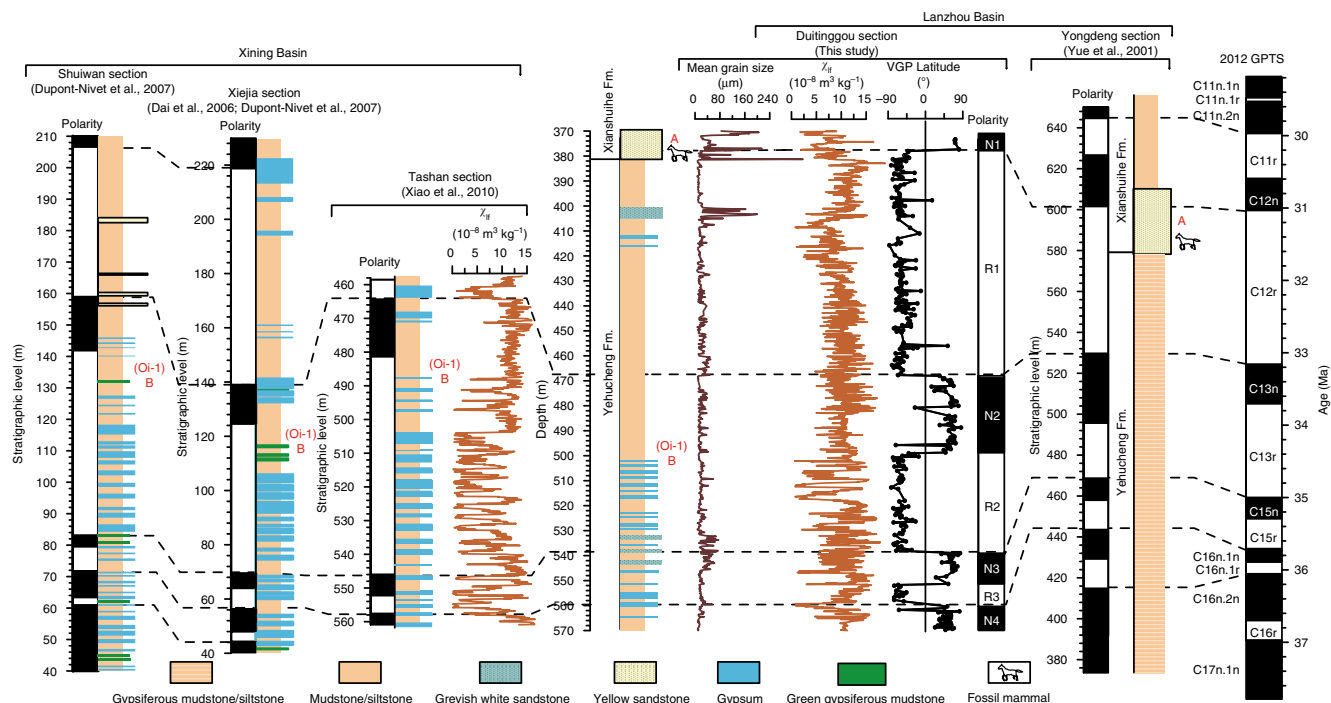


Fig. 2 Regional lithostratigraphic and magnetostratigraphic correlations. Lithostratigraphy and magnetostratigraphy of the Duitinggou and Yongdeng³⁶ sections in the Lanzhou Basin are compared with those of the Shuiwan⁹, Tashan¹⁶, and Xiejia^{9,40} sections in the Xining Basin, and correlate with the 2012 geomagnetic polarity time scale (GPTS)⁴¹. Mean grain size and magnetic susceptibility (χ_{lf}) records for the Duitinggou section and the Tashan χ_{lf} record¹⁶ are also shown. The uppermost 14 virtual geomagnetic pole (VGP) latitudes (open circles) for the Duitinggou section are from the bottom of the Xianshuihe Formation³⁷. The yellow sand layer (layer A) that overlies the Yehucheng Formation at the Duitinggou and Yongdeng sections is a prominent marker layer across the Lanzhou Basin. The Oi-1 event coincides with the end of regular alternations of gypsum and red mudstone/siltstone beds at gypsum (or green gypsiferous mudstone) layer B, and with a decreased amplitude variability of χ_{lf} at 100-kyr eccentricity periods. The Yehucheng Formation in the Yongdeng section was described only as gypsiferous mudstone/siltstone; more detailed lithological variations were not reported by Yue et al.³⁶.

(Fig. 2). This supports the correlation of the thick reversed polarity zone R1 of the upper Yehucheng Formation underlying marker layer A to reversed polarity chron C12r. In both the Lanzhou and Xining basins, regularly cyclic gypsum beds were present during the late Eocene and disappeared just prior to normal polarity chron C13n. This supports the correlation of thick reversed polarity zone R2 to reversed polarity chron C13r. Regional stratigraphic correlations, biostratigraphic constraints, and clear correlation with the GPTS together indicate that the normal polarity zone N2 between R1 and R2 correlates with normal polarity chron C13n (Fig. 2; Supplementary Note 1; Supplementary Fig. 4).

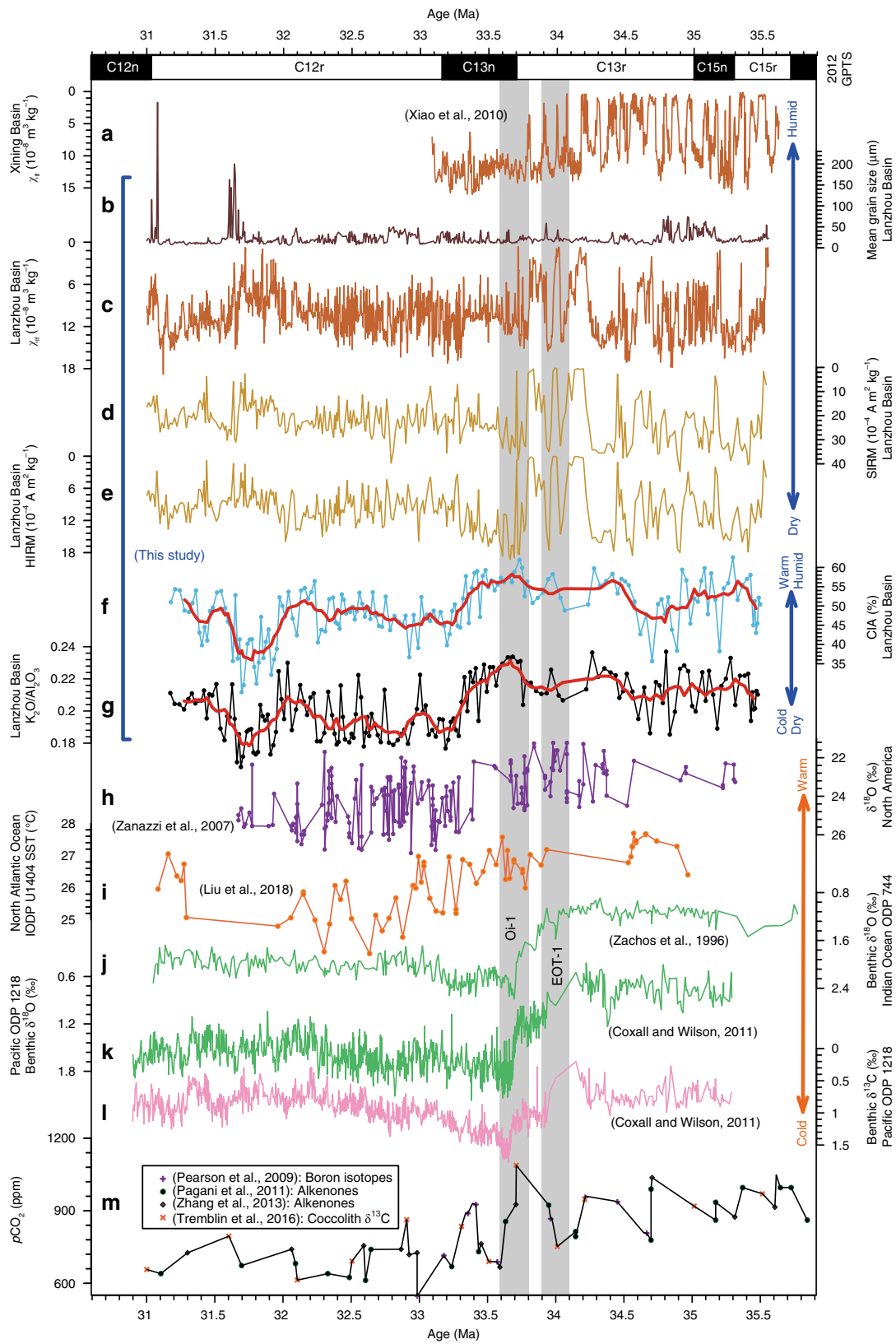
Palaeoclimatic records of the EOT from the Lanzhou Basin.

Detailed magnetic and mineralogical analyses (Supplementary Figs. 5 and 7–12) suggest that low-frequency magnetic susceptibility (χ_{lf}) of playa-palaeolake deposits in the Lanzhou Basin reflects primarily magnetic mineral concentration changes (see Supplementary Note 2 for details). The χ_{lf} record has a higher resolution than the saturation isothermal remanent magnetization (SIRM), and hard isothermal remanent magnetization (HIRM) records, but they all vary consistently throughout the section (Supplementary Fig. 12). As is the case in the Xining Basin^{9,16}, their values are low in gypsum and siltstone layers, which represent perennial playa lake to alluvial anoxic subaqueous conditions with high precipitation. Such conditions probably facilitated partial post-depositional magnetite and hematite dissolution and gypsum formation that diluted the magnetic expression. They also potentially drove rapid clastic material transportation to the playa lake from catchment regions; potential subaerial exposure had shorter durations that limited pedogenic processes during and after deposition. This would have limited pedogenic magnetic mineral

formation. In contrast, the χ_{lf} values are high in red mudstone beds, which represent lake retreat and oxic distal alluvial fan subaerial conditions with low precipitation. Such conditions would have increased pedogenic magnetic mineral formation during increased ephemeral subaerial exposure. The presence of pedogenic superparamagnetic (SP) particles is suggested by first-order reversal curve (FORC) diagrams⁴² and a positive linear correlation between frequency-dependent magnetic susceptibility (χ_{fd}) and χ_{lf} (Supplementary Figs. 9, 10). Oxic distal alluvial fan conditions also facilitated detrital magnetic mineral preservation during deposition. Moreover, gypsum beds disappeared and dilution of non-magnetic materials decreased substantially (see Supplementary Note 2 for details; Supplementary Fig. 13).

Thus, combined pedogenic, dissolution, dilution, and preservation effects provide a plausible model to explain notable orbital-scale χ_{lf} changes of the Lanzhou Basin fluvial-lacustrine sediments. As observed in sedimentary, clay mineral, and pollen studies in the Xining Basin^{9,14,16–18}, low χ_{lf} units in the Lanzhou Basin, which are indicative of low magnetic mineral concentrations, are also related to high regional precipitation based on our likely combined mechanism, and vice versa (Supplementary Fig. 13). With the χ_{lf} record providing a past hydroclimate proxy, we further refined the magnetochronology by tuning the 405-kyr and 100-kyr components in our χ_{lf} record to Earth's computed orbital eccentricity record⁴³ (see “Methods” for details; Supplementary Figs. 14–16). Below we assess NE Tibetan Plateau terrestrial climate evolution across the EOT using environmental magnetic and element-based chemical weathering records using our refined astronomical time scale.

The χ_{lf} , SIRM, and HIRM records are all characterized by a shift at ~ 33.7 Ma (Fig. 3c–e), which coincides with a lithological



shift (Fig. 2). Consistently higher amplitude variability is observed with a 100-kyr eccentricity period before ~33.7 Ma (Fig. 3c–e), which is also notable in the Xining Basin χ_{lf} record (Fig. 3a). The long-term χ_{lf} time series of the Duitingou section has an average resolution of 2.5 kyr between 31.0 and 35.5 Ma, with a typical

resolution between ~2 and 5 kyr before 33.7 Ma and between ~1 and 4 kyr after 33.7 Ma (Supplementary Fig. 16h). The resolution is sufficient to assess orbital variability in the obliquity band (41-kyr), while more tentative indications can be obtained for the precession band (~23-kyr). Spectral analysis of the χ_{lf} record

Fig. 3 Global and terrestrial climate changes across the Eocene–Oligocene transition (EOT). **a** Low-frequency magnetic susceptibility (χ_{lf}) for the Tashan section, Xining Basin¹⁶. **b** Mean grain size, **c** χ_{lf} , **d** saturation isothermal remanent magnetization (SIRM), **e** hard isothermal remanent magnetization (HIRM), **f** chemical index of alteration (CIA), and **g** K_2O/Al_2O_3 records from Lanzhou Basin playa-palaeolake sediments. Age models for both the Lanzhou and Xining records were established first by magnetostratigraphy and were then refined by matching 405-kyr and 100-kyr components in the χ_{lf} record with the computed record of Earth's orbital eccentricity⁴³. **h** $\delta^{18}O$ record of fossil remains from central North America¹³. **i** Sea surface temperature (SST) from IODP U1404, North Atlantic Ocean, based on alkenone unsaturation index¹⁵. **j** Benthic foraminiferal $\delta^{18}O$ from ODP Site 744, southern Indian Ocean⁵². **k, l** Benthic foraminiferal $\delta^{18}O$ and $\delta^{13}C$ from ODP Site 1218, tropical Pacific Ocean⁵. The two increasing $\delta^{18}O$ and $\delta^{13}C$ steps are designated as EOT-1 and Oi-1, respectively. **m** Atmospheric pCO_2 reconstruction across the EOT from ODP Site 925/929 with coccolith $\delta^{13}C$, boron isotopes, and alkenones^{53–56}.

suggests strong expression in the 405-kyr and 100-kyr bands throughout the ~35.3–31.3 Ma interval (Fig. 4a–c). Notably, after ~33.7 Ma, there is a strong obliquity expression, with a relatively weaker precession expression, and the obliquity amplitude-modulated 1.2 Myr band is observed superimposed on the 100 and 405-kyr bands (Fig. 4a–c). Similar orbital variability is observed in the spectral evolution of 3-point and 5-point running χ_{lf} means, which suppresses potential short-term noisy signals (Supplementary Fig. 17). These orbital climate variations, particularly the orbital expression shift at 33.7 Ma, are also evident in the depth domain and in the untuned magnetostratigraphy (Supplementary Figs. 14, 15). This confirms the robustness of the orbital response shift of the Lanzhou Basin climate identified across Oi-1. We note that in the untuned magnetostratigraphy the calculated eccentricity, obliquity, and/or precession bands are displaced slightly or have a subdued expression in a few intervals where a non-orbital signal structure appears to be more prominent (Supplementary Fig. 15). In our refined astronomical time scale, orbital expression (eccentricity, obliquity, and precession) in the χ_{lf} record is enhanced significantly, and non-orbital noise is substantially lower (Fig. 4c) relative to the untuned magnetostratigraphy (Supplementary Fig. 15).

The chemical index of alteration (CIA, the molar ratio of Al_2O_3 to $Al_2O_3 + CaO + Na_2O + K_2O$) and the K_2O/Al_2O_3 ratio are two classic chemical weathering proxies; they correlate positively with chemical weathering intensity^{44,45}. They vary consistently during the late Eocene–early Oligocene (Fig. 3f–g), and correlate linearly with each other (Supplementary Fig. 18). While the CIA and K_2O/Al_2O_3 records have much lower sampling resolution and cannot capture detailed orbital variability like the high-resolution χ_{lf} record, some 100-kyr cycles are roughly evident in both chemical weathering records before ~34.6 Ma and after ~32.8 Ma (Fig. 3f–g). Notably, the negative CIA and K_2O/Al_2O_3 shifts from ~33.7 to 33.2 Ma indicate a substantial chemical weathering intensity decrease in the Lanzhou Basin (Fig. 3f–g), consistent with a change from more intensive weathering under higher temperature and precipitation conditions to insignificant alteration under lower temperature and precipitation conditions across the Oi-1 event^{44,45}. The observed shifts cannot be explained in terms of grain size changes because CIA and K_2O/Al_2O_3 correlate poorly with mean grain size (Supplementary Fig. 18d, e). Moreover, grain size does not shift at 33.7–33.2 Ma (Fig. 3b).

Discussion

Our high-resolution records indicate that orbitally paced variability was evident for the late Eocene–early Oligocene NE Tibetan Plateau climate. Consistent with the Lanzhou Basin χ_{lf} record (Fig. 4a–c), spectral analysis of the high-resolution Pacific benthic $\delta^{18}O$ record also indicates a strong eccentricity (405- and 100-kyr) band throughout the late Eocene–early Oligocene between ~35.1 and 31.3 Ma, and a superimposed strong obliquity and obliquity amplitude-modulated band of 1.2 Myr after 33.7 Ma, together with a relatively weaker and discontinuous precession expression (Fig. 4d–f). In the benthic marine $\delta^{18}O$ record, strong 405 and 100-kyr eccentricity bands persist continuously through at least the

Middle Miocene^{11,30,31}. The Xining Basin χ_{lf} record has 22 regular large-amplitude cycles from polarity chrons C15r to C13r (Fig. 3a), with durations of 1.666 Myr (35.404–33.738 Ma) in the 2004 GPTS⁴⁶ and 2.001 Myr (35.706–33.705 Ma) in the updated 2012 GPTS⁴¹, respectively. The 22 χ_{lf} cycles correspond to a 76-kyr periodicity based on the 2004 GPTS⁴⁶, which were interpreted previously as due to eccentricity⁹, obliquity¹⁶, or a combination of obliquity and eccentricity cycles³². However, these cycles have a 91-kyr periodicity in an age model based on the 2012 GPTS⁴¹, which is consistent with eccentricity cycles. Spectral analyses of the Xining Basin χ_{lf} record using the refined astronomical chronology suggest pronounced eccentricity (100 and 405-kyr) rhythms between 35.3 and 33.3 Ma (Supplementary Fig. 19). Furthermore, the Maoming Basin (South China) lithological record has strong latest Eocene eccentricity cycles¹⁹. Thus, the Lanzhou Basin χ_{lf} and Pacific benthic $\delta^{18}O$ records suggest that NE Tibetan Plateau and global changes were consistently paced by eccentricity both before and after the onset of major Antarctic glaciation, consistent with the heartbeat of the Earth system as paced by eccentricity cycles^{11,30,31,47}.

Appearance in spectral analyses of strong obliquity cyclicity and of a 1.2-Myr obliquity-amplitude-modulated band after 33.7 Ma in both the Lanzhou Basin χ_{lf} and Pacific benthic $\delta^{18}O$ records (Fig. 4) indicates that Asian climate and Antarctic ice sheets started to respond dynamically to obliquity forcing across Oi-1. Likewise, strong obliquity cyclicity was also absent before 33.7 Ma and appeared clearly in the Xining Basin χ_{lf} record after this time (Supplementary Fig. 19). Cyclostratigraphy in the Maoming Basin lithology¹⁹ seems to suggest a similar shift from dominantly eccentricity to obliquity cycles across Oi-1. Accordingly, it appears that this obliquity response was not significant in the latest Eocene when major Antarctic ice sheets were not established. In addition to obliquity cyclicity, the precession signal also appeared clearly after ~33.7 Ma in the spectral analyses of the Lanzhou Basin χ_{lf} record (Fig. 4). This orbital shift also seems to be present in the Pacific benthic $\delta^{18}O$ record⁵, although the precession band is weaker and less continuous (Fig. 4). The resolution of the Lanzhou Basin χ_{lf} record (Supplementary Fig. 16h) is in principle sufficient to reveal the precession band before 33.7 Ma. While detailed sedimentary observations did not yield evidence for hiatuses in the late Eocene–early Oligocene Duitinggou section, occasional unidentified small hiatuses or sedimentation rate decreases may cause one or several precession cycles to be (partially) missed in a few intervals. However, they are unlikely to have been missed throughout the whole ~2-Myr long interval between 35.5 and 33.7 Ma (Supplementary Note 3), especially when a clear precession expression is observed after 33.7 Ma. Thus, such a precessional expression shift across the Oi-1 event in the Lanzhou Basin χ_{lf} record is unlikely related to sedimentation rate changes. We note, however, that validation from even more highly resolved multiple proxy records would be ideal.

Environmental smoothing related to post-depositional diagenesis and biological disturbance^{48–50} is another potential factor that can influence orbital variability expressions in low sedimentation

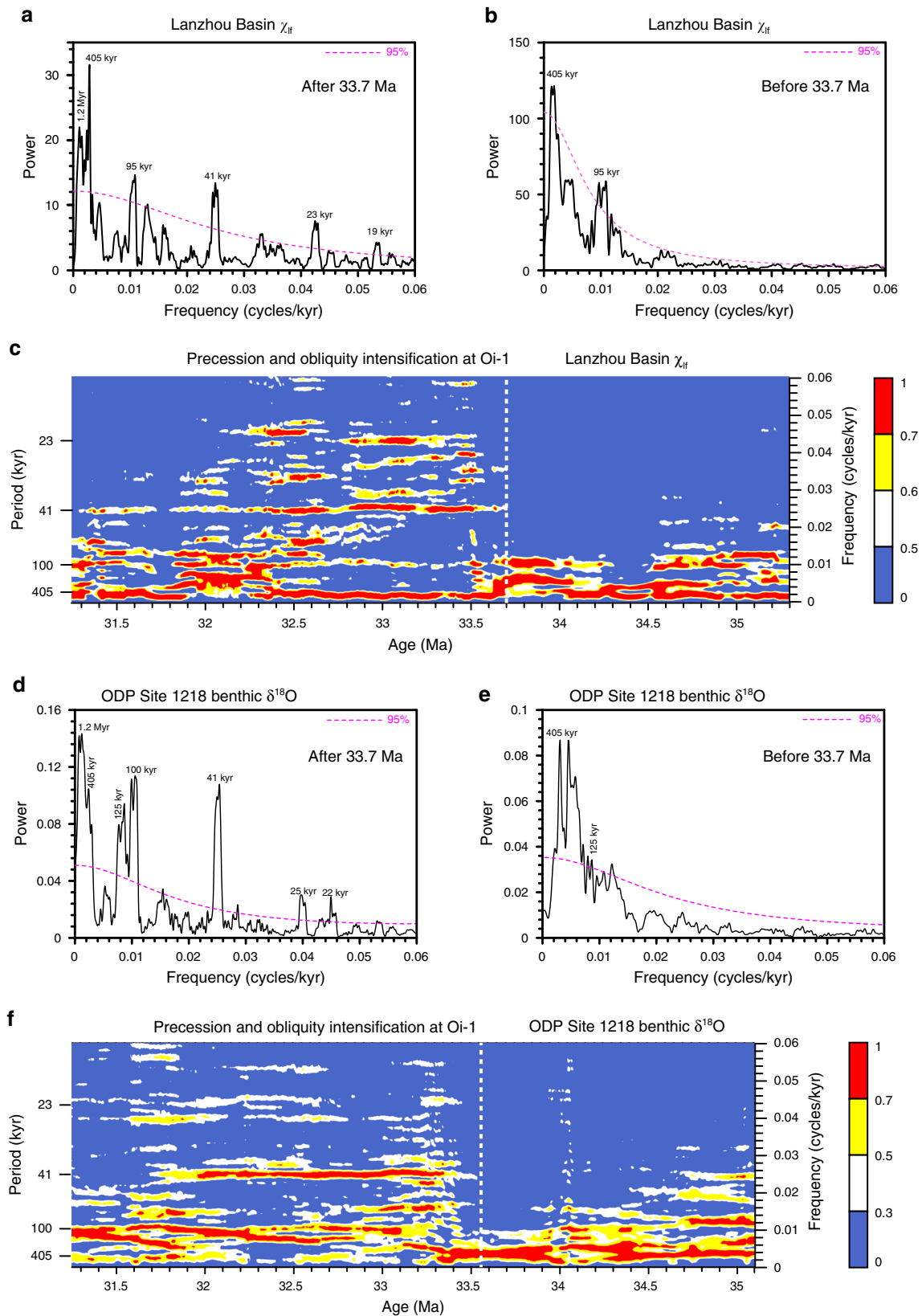


Fig. 4 Orbital climate variability across the Eocene-Oligocene transition. 2π -Multi-taper method (MTM) power spectrum of (a, b) Lanzhou Basin χ_{ff} and (d, e) ODP Site 1218 benthic $\delta^{18}O$ records after and before 33.7 Ma, with a robust red-noise model at the 95% confidence level. Spectral evolution for (c) Lanzhou Basin χ_{ff} and (f) ODP Site 1218 benthic $\delta^{18}O$ records calculated using the MATLAB Evoffte routine, with a 600-kyr sliding window and 2-kyr sliding step.

rate records. However, it is unlikely to have affected significantly the Lanzhou playa-palaeolake sediments as suggested by the absence of root and burrow marks and by the preservation of centrimetric laminar mudstone and gypsum beds before 33.7 Ma (Supplementary Fig. 3d–g). Moreover, bioturbation is largely restricted to a narrow depth of surficial sediments, which varies from <3 cm for varved and laminated lake sediments to ~12 cm for homogenous massive lake sediments in wet regions^{49,50}. Thus, bioturbational mixing depths for Lanzhou palaeolake sediments in arid western China with low organic content are expected to be smaller, probably one to two orders of magnitude smaller than the expected thickness of precession (70–100 cm) and obliquity (150–190 cm) cycles (Supplementary Fig. 14). In addition, evident precession and obliquity cycles are absent between 35 and 33.7 Ma from terrestrial records from Xining (Supplementary Fig. 19) and Maoming¹⁹ basins, the marine ODP Site 1218 benthic $\delta^{18}\text{O}$ record (Fig. 4), and the high-resolution X-ray fluorescence (XRF) core scanning Si, Ca, and Fe records⁴⁷ for ODP Sites 1218, U1333, and U1334. All of these terrestrial and marine records are instead dominated consistently by eccentricity. More detailed discussion in Supplementary Note 3 documents that the absence of apparent precession and obliquity expressions between 35 and 33.7 Ma in the Lanzhou Basin χ_{lf} record is unlikely to have been caused by sedimentation rate/environmental smoothing variations or by unidentified small hiatuses. As summarized in a flowchart of our orbital tuning strategy (Supplementary Fig. 20), we conclude that the orbital response shift identified at ~33.7 Ma in the Lanzhou Basin χ_{lf} record is a robust feature of Asian climate reorganization across Oi-1, which is supported by (1) the Maoming cyclostratigraphy¹⁹ and spectral analyses of (2) the Lanzhou Basin χ_{lf} record in the depth domain (Supplementary Fig. 14), and in astronomical and magnetostratigraphic time scales (Fig. 4; Supplementary Fig. 15), (3) the Xining χ_{lf} record (Supplementary Fig. 19), and (4) the ODP Site 1218 benthic $\delta^{18}\text{O}$ record (Fig. 4). In addition, a similar hydroclimate transition from eccentricity to combined eccentricity, obliquity, and precession pacing is observed in the Qaidam Basin, NE Tibetan Plateau, at ~8.5 Ma when the global climate cooled and Antarctic glaciation intensified⁵¹.

The long-term trend in our records confirms previous inferences about Asian aridification and cooling across the EOT^{9,14,16–21,23}. The higher resolution of our records constrains more precisely the age of the main transition to ~33.7 Ma, around the C13r–C13n boundary, which corresponds with the Oi-1 event (33.8–33.6 Ma) in high-resolution marine benthic $\delta^{18}\text{O}$ and $\delta^{13}\text{C}$ records^{5,52}, and post-dates the initial EOT-1 event at 34.1–33.9 Ma (Fig. 3). Sharp termination of periodic gypsum deposition at around the C13r–C13n boundary at ~33.7 Ma in the Lanzhou Basin and ~33.8 Ma in the Xining Basin, along with a shift to lower χ_{lf} SIRM, and HIRM minima, suggest a major shift to lower precipitation and to a smaller and/or shallower lake exactly during Oi-1 (Fig. 3). Earlier and less substantial aridification is suggested by decreasing gypsum bed thicknesses and associated low- χ_{lf} peaks at ~34.07 Ma in the Xining Basin possibly in correspondence with the EOT-1 event¹⁶, which is not clearly expressed in the Lanzhou Basin records. This early change likely was more subtle than the later, region-wide change at 33.8–33.7 Ma, so the stronger Xining Basin expression compared to the Lanzhou Basin may reflect local variations in climate drivers and/or basin sensitivity to these drivers. In contrast, the later change at Oi-1 was large enough to produce unambiguous, major regional impacts. Consistent with the timing of major lithological and environmental magnetic shifts in the Lanzhou Basin, the negative CIA and $\text{K}_2\text{O}/\text{Al}_2\text{O}_3$ shifts that started at ~33.7 Ma and that were amplified at ~33.3 Ma indicate a prominently decreasing chemical weathering trend with drier and cooler terrestrial climate starting at the Oi-1 event (Fig. 3f–g), which was possibly accompanied by aeolian input increases³². The

CIA and $\text{K}_2\text{O}/\text{Al}_2\text{O}_3$ records have much lower sampling resolution and, thus, cannot be compared directly with the χ_{lf} record over short orbital (precessional) time scales for some intervals. However, these low-resolution chemical weathering proxies provide interpretable long-term trend changes consistent with that of the χ_{lf} record, which is supported by positive correlations of χ_{lf} with CIA and $\text{K}_2\text{O}/\text{Al}_2\text{O}_3$ (Supplementary Fig. 18b, c).

Pronounced NE Tibetan Plateau hydroclimate changes during Oi-1, including an orbital response shift and enhanced aridification and cooling, may have been linked to the coeval global climate reorganization. Although CO_2 reconstructions^{53–56} lack the resolution and precise chronological constraints needed for detailed comparison with our records, they suggest that CO_2 probably dropped by >300 ppm during Oi-1, which is more than during EOT-1 (Fig. 3m). Ice-sheet-climate modelling results^{2,57,58} indicate that the major CO_2 drop during Oi-1 may have been a primary driver for Antarctic ice-sheet expansion to the coastline at *ca* 33.7 Ma³.

We link the marked climatic transition on the NE Tibetan Plateau that started during Oi-1 to the associated larger CO_2 drop and full Antarctic glaciation. Accordingly, atmospheric CO_2 -driven global cooling^{54,57} resulted in less atmospheric moisture under lower temperatures and weaker summer monsoonal circulation¹⁰, which would have decreased moisture transport to the NE Tibetan Plateau by the summer monsoon from the northern Indian and western Pacific Oceans, and by the Westerlies from the proto-Paratethys Sea that extended over Eurasia during this time³². Palaeoclimate reconstructions and modelling results both suggest that Antarctic ice-sheet growth would have caused southern hemisphere Westerlies to intensify and shift northward to increase cold Southern Ocean bottom and intermediate water transportation to northern hemisphere ocean basins^{3,6,7,59}. The large (>50 m) global mean sea-level lowering³ due to major Antarctic glaciation would have also exposed northern Indian and western Pacific Ocean continental shelves, and caused westward retreat of the giant, shallow proto-Paratethys Sea. This large-scale oceanic retreat decreased moisture supply to the NE Tibetan Plateau^{9,60} and led to more continental central Asian climates with cooler winters^{61,62}. The contemporaneity of major Antarctic glaciation and sea-level lowering during Oi-1 with rapid Asian aridification is supported by the sharp termination of periodic gypsum beds in both the Lanzhou and Xining basins. The subsequent long-term trend of Antarctic deglaciation and sea-level rise from ~33.6 to 31.7 Ma may have driven partial recovery of NE Tibetan Plateau precipitation as indicated by a modest long-term decline in the Lanzhou Basin χ_{lf} , SIRM, and HIRM records (Fig. 3c–e).

After their development at Oi-1, extensive Antarctic ice sheets during the lower- CO_2 early Oligocene responded dynamically to high-latitude southern hemisphere summer insolation variations with strong precession and obliquity cycles. Under the competing influence of the Asian summer monsoon and Westerlies^{9,10}, moisture availability in the semi-arid Lanzhou Basin varied consistently with orbital Antarctic ice-sheet forcing. Although the environmental background differed significantly from Quaternary glacial-interglacial cycles, which were dominated by both Antarctic and northern hemisphere ice-sheet variability, Oligocene glacial-interglacial Antarctic ice-sheet advances and retreats over precession and obliquity cycles in response to summer insolation may have influenced orbital variability of Asian terrestrial climate by potential variations in sea level, atmospheric and oceanic circulation, CO_2 , and temperature^{3,11}. Accordingly, during glacial intervals, lowered sea level would have increased the land area, thus lengthening the moisture transportation pathway of the Asian summer monsoon from the northern Indian and western Pacific Oceans to the NE Tibetan Plateau. In particular,

the proto-Paratethys Sea retreat may have lengthened markedly the transport pathway of the Westerlies^{9,60}. Both would have reduced moisture transport to the NE Tibetan Plateau. In addition, lower CO₂ levels and temperatures would have reduced atmospheric water vapour formation in the northern Indian and western Pacific Oceans and the proto-Paratethys Sea during glacial. Accordingly, a decreased oceanic moisture supply during Oligocene glacials also played a role. These large-scale processes may have reversed during interglacials and led to relatively wetter climates. Thus, we infer that links of Asian climate variations with global climate system were enhanced after the Oi-1 event not only because of sensitivity to larger orbitally driven Antarctic ice-sheet variations, but also because of increased sensitivity to regional insolation forcing in a lower-CO₂ Oligocene icehouse world.

In summary, we conclude that, coinciding closely with the Oi-1 event, precipitation variability on the NE Tibetan Plateau shifted from being dominantly eccentricity-paced to responding to combined eccentricity, obliquity, and precession forcing. Such an orbital response shift is also evident for the wider global climate as suggested by the marine benthic $\delta^{18}\text{O}$ record. The NE Tibetan Plateau also experienced a major increase in aridification and cooling during Oi-1. We relate these pronounced changes in orbital climate variability, aridification, and cooling on the NE Tibetan Plateau to changed climatic boundary conditions across Oi-1, including a major CO₂ drop and development of continental-scale Antarctic ice sheets, which reorganized atmospheric and oceanic circulation along with global climate, including the terrestrial Asian climate system.

Methods

Sampling. To obtain samples that were as fresh as possible and to decrease the potential influence of recent weathering, the weathered outcrop surface was removed (at least the topmost 20 cm) before collecting samples from freshly exposed sediment. For magnetostratigraphic analysis, 510 block samples were collected at 30–40-cm stratigraphic intervals and were oriented in the field with a compass. Two cubic samples (2 cm × 2 cm × 2 cm) were taken from each oriented block for thermal demagnetization treatment to establish a magnetostratigraphy. Some leftovers of these block samples were further used for mineral magnetic and elemental measurements. A total of 2001 unoriented samples were collected for climate proxy measurements at 10-cm intervals. All experiments were carried out at the Institute of Earth Environment, Chinese Academy of Sciences, Xi'an, China.

Palaeomagnetic analyses. Stepwise thermal demagnetization of the natural remanent magnetization (NRM) was conducted using a TD-48 thermal demagnetizer. 510 oriented cubic samples (one per level) were stepwise heated at 18 successive steps with 10–50 °C temperature increments to a maximum temperature of 680 °C. After each demagnetization step, the remaining NRM was measured with a 2-G Enterprises Model 755-R cryogenic magnetometer housed in a magnetically shielded space. The NRM intensity of samples is usually of the order of 10⁻³–10⁻² A/m; the instrument background (or noise) level in the magnetometer is <10⁻⁶ A/m. Demagnetization results were evaluated using orthogonal diagrams⁶³; the principal component direction for each sample was computed using least-squares linear fitting⁶⁴. Principal component analysis (PCA) was performed using the PaleoMag software⁶⁵; PCA fits were not anchored to the origin of orthogonal diagrams⁶⁶.

Detailed palaeomagnetic analysis of stepwise thermal demagnetization results enabled us to construct a robust magnetostratigraphic chronology for the Duitingou section. After removal of a secondary overprint isolated by progressive demagnetization to 250–350 °C (sometimes up to 400–450 °C), a characteristic remanent magnetization (ChRM) was isolated up to 680 °C (Supplementary Fig. 5). ChRM directions were determined using strict selection criteria. At least four (but typically 8–15) consecutive demagnetization steps that decay linearly toward the origin of orthogonal diagrams were used to determine the ChRM direction from 250–350 °C to 680 °C (sometimes from 400–450 °C to 680 °C), with maximum angular deviation (MAD) values ≤15° for line fits (not anchored to the origin). Polarity zones were defined here using at least three successive virtual geomagnetic pole (VGP) latitudes of identical polarity, which were calculated from ChRM directions. A few intervals with only a single palaeomagnetic direction may indicate a short-lived geomagnetic anomaly with ambiguous origin (cryptochrons) or a geomagnetic excursion^{60,67}, which need to be documented as a global feature before being considered as real, and were thus not used for determining the polarity zone and for calculating the overall mean direction. A few samples possibly

recorded a transitional geomagnetic field, with large ChRM direction divergences from the mean, and were also not used for polarity zone determination.

Mineral magnetic measurements. All 2001 unoriented samples were powdered and were then packed into non-magnetic cubic boxes (2 cm × 2 cm × 2 cm) for low-frequency magnetic susceptibility (χ_{lf}) and high-frequency magnetic susceptibility (χ_{hf}) measurements in the laboratory with a Bartington Instruments MS2 magnetic susceptibility meter. χ_{lf} and χ_{hf} were measured at 470 and 4700 Hz, respectively. Frequency-dependent magnetic susceptibility ($\chi_{fd} = \chi_{lf} - \chi_{hf}$) was calculated. We selected 363 samples at a 50 cm stratigraphic interval for isothermal remanent magnetization (IRM) measurements. Saturation IRM (SIRM) was imparted in a 2.5 oT field with an impulse magnetizer (model IM-10-30) and was measured with an AGICO JR-6A dual-speed spinner magnetometer in a magnetically shielded laboratory. After SIRM measurement, we further measured backfield IRM imparted at 0.3 T (IRM_{300mT}) by reversing the orientation of samples to calculate the hard IRM (HIRM): HIRM = (SIRM + IRM_{300mT})/2. IRM acquisition curves were also measured at 30 field steps up to 2.7 T for three typical samples.

Manually prepared magnetic extracts were made from five selected samples using a strong rare-earth magnet. FORC measurements of original samples and their magnetic extracts were made using a Princeton Measurements Corporation (Model 3900) vibrating sample magnetometer (VSM). For each sample, 80 FORCs were measured at fields up to ~300 mT, 100 ms averaging time, and 0.3 mT field increment. FORC data were processed using the FORCinel package⁶⁸. Low-temperature magnetic measurements of magnetic extracts were conducted with a Quantum Design superconducting quantum interference device (SQUID) Magnetic Properties Measurement System (MPMS). After cooling in a 5 T field from 300 to 5 K, a low-temperature SIRM, which was imparted in a 5 T field at 5 K, was measured from 5 to 300 K. Then a room temperature SIRM, which was imparted in a 5 T field at 300 K, was measured from 300 to 5 K and back to 300 K in zero field.

Mineralogical analyses. Morphological and mineral composition analyses of magnetic extracts were performed using a ZEISS EVO-08 scanning electron microscope (SEM) equipped with a Bruker X-ray energy dispersive spectroscope (EDS). Magnetic extracts were mixed with a low viscosity epoxy and were dispersed by ultrasonication, followed by vacuum-impregnation for 20 min. After curing at 40 °C for 10 h, the specimens were ground with emery paper with successively finer grit size up to 7000 grade and were polished using cloths embedded with 1 μm diamond abrasive. After polishing, the specimens were cleaned ultrasonically in acetone for ~20 min. Finally, the flat polished specimens were coated with a gold layer using an evaporative coater. The polished magnetic extract specimens were then used to determine the morphology of individual particles (including shape and size distributions) and their mineral compositions using the SEM-EDS system^{69,70}. Each backscattered electron (BSE) image was obtained with an accelerating voltage of 20 kV and a beam current of 100 μA. The particle size distribution was obtained from 30 BSE pictures from different areas of each polished specimen. An X-ray spectrum was collected for 10 min for each BSE image, and an X-ray dotted map (30 BSE pictures) for each sample was acquired for ~5 h for all chemical elements recognized. X-ray spectra were used to determine the mineral compositions by calculating the net X-ray peak-area of each element⁶⁹. The X-ray maps, with a concentration detection sensitivity of 1%, were used to detect the spatial mineral distributions.

Elemental measurements. Elemental analyses were performed on 175 bulk samples. About 5 g of each sample was dried at 40 °C for 24 h with subsequent grinding to <38 μm (passing a 200-mesh sieve) with an agate mortar and pestle. Powders were then compacted into an oblate polyethylene disc (32-mm diameter) with a tablet machine. The discs were used to determine major element concentrations with an Axios advanced wavelength dispersive X-ray fluorescence instrument (WD-XRF; PANalytical, Ea Almelo, The Netherlands). Relative standard deviations from repeated analyses of the National Standard GSS-8 and GSD-12 were below 2% for all major elements. Grain size analyses were conducted on 768 bulk samples. After removal of organic matter by 10% H₂O₂ and carbonate by 10% HCl, samples were measured using a Malvern 2000 laser instrument.

Astronomical time scale and spectral analyses. We used an automatic orbital tuning approach⁷¹ to generate an astronomical time scale. We used the 2π-Multi-Taper Method (MTM) to analyze the power spectra with the function Spectral Analysis⁷². Evolutionary power spectra were calculated using the MATLAB Eovffite routine. Both power spectra and evolutionary power spectra were analysed using the Acycle software⁷³.

A magnetostratigraphy for the Duitingou section was first established by linear interpolation, based on the ages of the C12r–C12n, C13n–C12r, C13r–C13n, C15n–C13r, C15r–C15n, and C16n.1n–C15r reversal boundaries from the 2012 GPTS⁴¹. We then conducted spectral analyses of the Lanzhou Basin χ_{lf} record in the depth domain and using the untuned magnetostratigraphy before tuning, which suggested continuous 405-kyr and 100-kyr eccentricity bands throughout the late Eocene–early Oligocene (Supplementary Figs. 14, 15). Accordingly, we first tuned the 405-kyr component filtered from the χ_{lf} record to long (405-kyr) eccentricity in the astronomical solution⁴³ to achieve a cycle-by-cycle correlation within

magnetostratigraphical constraints. Generally, low 405-kyr χ_{lr} peaks associated with wet climates were tuned to long (405-kyr) eccentricity maxima (Supplementary Fig. 16). We then further refined the age model by fine-adjustment of individual 100-kyr cycles. Low 100-kyr χ_{lr} peaks (wet climates) were tuned to short (100-kyr) eccentricity maxima within the 405-kyr tuned constraints. To optimize tuning, ages for palaeomagnetic reversals and for 405-kyr tuning were not kept fixed. However, for a few intervals (e.g., ~32.6–33.5 Ma) with stronger 405-kyr variability than 100-kyr variability, the 405-kyr matches were given preference, with simultaneous consideration of resulting sedimentation rate changes, to avoid over-tuning during the 100-kyr tuning stage.

We considered >50 different tuning options for the Duitinggou χ_{lr} record using age correlation points where high- χ_{lr} peaks facilitated consistent correlation point selection. Some (~10) of these options resulted in either high 405-kyr correlations but low 100-kyr correlations or high 100-kyr correlations but low 405-kyr correlations within the uncertainty of the magnetostratigraphy. Some (~5) produced both high 405-kyr and 100-kyr correlations, but caused the palaeomagnetic reversal ages to differ too much (up to > 500 kyr) from their GPTS ages. Together, these ~15 options were discarded. In the remaining ~35 options, both 405-kyr and 100-kyr components filtered from the χ_{lr} record correlate cycle-by-cycle with the target curves, sedimentation rates vary reasonably, and the ages of palaeomagnetic reversals, within uncertainty, are generally consistent with their GPTS ages. All ~35 options produce a similar major spectral evolutionary feature for the χ_{lr} record, which is characterized by a transition across Oi-1 from dominantly eccentricity to a combination of eccentricity, obliquity, and precession, although the evolutionary intensity and time of each orbital signal vary in different options. From them, we selected the mostly likely option, which contained minimal (42) age correlation points but resulted simultaneously in the high correlation of both the 405-kyr and 100-kyr χ_{lr} components with their target curves, high consistency of palaeomagnetic reversal age with their GPTS ages, and consistent sedimentation rate changes with lithology (Supplementary Fig. 16; Supplementary Tables 1 and 2). All ~35 options were used to estimate age uncertainties for the tie points. The selected 42 tie points were moved largest forward (older limit) and backward (younger limit) to contain all ~35 possible correlation options to estimate potential positive and negative age uncertainties, respectively.

Data availability

All data presented this study are accessible openly at the National Tibetan Plateau Data Center (<https://data.tpdc.ac.cn/en/data/e3d2b9e4-53d9-4b49-8da9-9c3d5a7b458c>).

Code availability

Code for orbital tuning and spectral analysis used in this research is available from the corresponding author upon request.

Received: 6 June 2019; Accepted: 16 September 2020;

Published online: 16 October 2020

References

- Zachos, J. C., Dickens, G. R. & Zeebe, R. E. An early Cenozoic perspective on greenhouse warming and carbon-cycle dynamics. *Nature* **451**, 279–283 (2008).
- Ladant, J. B., Donnadieu, Y., Lefebvre, V. & Dumas, C. The respective role of atmospheric carbon dioxide and orbital parameters on ice sheet evolution at the Eocene–Oligocene transition. *Paleoceanography* **29**, 810–823 (2014).
- Miller, K. G. et al. In *The Late Eocene Earth: Hothouse, Icehouse, and Impacts* (eds Koeberl, C. & Montanari, A.) 169–178 (Geological Society of America Special Publication, 2009).
- Coxall, H. K., Wilson, P. A., Pälike, H., Lear, C. H. & Backman, J. Rapid stepwise onset of Antarctic glaciation and deeper calcite compensation in the Pacific Ocean. *Nature* **433**, 53–57 (2005).
- Coxall, H. K. & Wilson, P. A. Early Oligocene glaciation and productivity in the eastern equatorial Pacific: insights into global carbon cycling. *Paleoceanography* **26**, PA2221 (2011).
- Coxall, H. K. et al. Export of nutrient rich Northern Component Water preceded early Oligocene Antarctic glaciation. *Nat. Geosci.* <https://doi.org/10.1038/s41561-018-0069-9> (2018).
- Goldner, A., Herold, N. & Huber, M. Antarctic glaciation caused ocean circulation changes at the Eocene–Oligocene transition. *Nature* **511**, 574–577 (2014).
- Pälike, H. et al. A Cenozoic record of the equatorial Pacific carbonate compensation depth. *Nature* **488**, 609–614 (2012).
- Dupont-Nivet, G. et al. Tibetan Plateau aridification linked to global cooling at the Eocene–Oligocene transition. *Nature* **445**, 635–638 (2007).
- Licht, A. et al. Asian monsoons in a late Eocene greenhouse world. *Nature* **513**, 501–506 (2014).
- Pälike, H. et al. The heartbeat of the Oligocene climate system. *Science* **314**, 1894–1898 (2006).
- Erhardt, A. M., Pälike, H. & Paytan, A. High-resolution record of export production in the eastern equatorial Pacific across the Eocene–Oligocene transition and relationships to global climatic records. *Paleoceanography* **28**, 130–142 (2013).
- Zanazzi, A., Kohn, M. J., MacFadden, B. J. & Terry, D. O. Large temperature drop across the Eocene–Oligocene transition in central North America. *Nature* **445**, 639–642 (2007).
- Page, M. et al. Synchronous cooling and decline in monsoonal rainfall in northeastern Tibet during the fall into the Oligocene icehouse. *Geology* **47**, 203–206 (2019).
- Liu, Z. H. et al. Transient temperature asymmetry between hemispheres in the Palaeogene Atlantic Ocean. *Nat. Geosci.* <https://doi.org/10.1038/s41561-018-0182-4> (2018).
- Xiao, G. Q., Abels, H. A., Yao, Z. Q., Dupont-Nivet, G. & Hilgen, F. J. Asian aridification linked to the first step of the Eocene–Oligocene climate Transition (EOT) in obliquity-dominated terrestrial records (Xining Basin, China). *Clim. Past* **6**, 501–513 (2010).
- Zhang, C. X. & Guo, Z. T. Clay mineral changes across the Eocene–Oligocene transition in the sedimentary sequence at Xining occurred prior to global cooling. *Palaeogeogr. Palaeoclimatol. Palaeoecol.* **411**, 18–29 (2014).
- Fang, X. M. et al. An Eocene–Miocene continuous rock magnetic record from the sediments in the Xining Basin, NW China: indication for Cenozoic persistent drying driven by global cooling and Tibetan Plateau uplift. *Geophys. J. Int.* **201**, 78–89 (2015).
- Li, Y. X. et al. Terrestrial responses of low-latitude Asia to the Eocene–Oligocene climate transition revealed by integrated chronostratigraphy. *Clim. Past* **12**, 255–272 (2016).
- Sun, J. M. et al. Synchronous turnover of flora, fauna, and climate at the Eocene–Oligocene boundary in Asia. *Sci. Rep.* **4**, 7463 (2014).
- Sun, J. M. & Windley, B. F. Onset of aridification by 34 Ma across the Eocene–Oligocene transition in Central Asia. *Geology* **43**, 1015–1018 (2015).
- Kraatz, B. P. & Geisler, J. H. Eocene–Oligocene transition in Central Asia and its effects on mammalian evolution. *Geology* **38**, 111–114 (2010).
- Fang, X. M. et al. Paleogene global cooling–induced temperature feedback on chemical weathering, as recorded in the northern Tibetan Plateau. *Geology* **47**, 992–996 (2019).
- Fan, M. J., Ayyash, S. A., Tripathi, A., Passey, B. H. & Griffith, E. M. Terrestrial cooling and changes in hydroclimate in the continental interior of the United States across the Eocene–Oligocene boundary. *Geo. Soc. Am. Bull.* **130**, 1073–1084 (2018).
- Colwyn, D. A. & Hren, M. T. An abrupt decrease in Southern Hemisphere terrestrial temperature during the Eocene–Oligocene transition. *Earth Planet. Sci. Lett.* **512**, 227–235 (2019).
- Hren, M. T. et al. Terrestrial cooling in Northern Europe during the Eocene–Oligocene transition. *Proc. Natl Acad. Sci. USA* **110**, 7562–7567 (2013).
- Katz, M. E. et al. Stepwise transition from the Eocene greenhouse to the Oligocene icehouse. *Nat. Geosci.* **1**, 329–334 (2008).
- Lear, C. H., Bailey, T. R., Pearson, P. N., Coxall, H. K. & Rosenthal, Y. Cooling and ice growth across the Eocene–Oligocene transition. *Geology* **36**, 251–254 (2008).
- Liu, Z. H. et al. Global cooling during the Eocene–Oligocene climate transition. *Science* **323**, 1187–1190 (2009).
- Levy, R. H. et al. Antarctic ice-sheet sensitivity to obliquity forcing enhanced through ocean connections. *Nat. Geosci.* **12**, 132–137 (2019).
- De Vleeschouwer, D., Vahlenkamp, M., Crucifix, M. & Pälike, H. Alternating Southern and Northern Hemisphere climate response to astronomical forcing during the past 35 m.y. *Geology* **45**, 375–378 (2017).
- Abels, H. A., Dupont-Nivet, G., Xiao, G. Q., Bosboom, R. & Krijgsman, W. Stepwise change of Asian interior climate preceding the Eocene–Oligocene Transition (EOT). *Palaeogeogr. Palaeoclimatol. Palaeoecol.* **299**, 399–412 (2011).
- Horton, B. K. et al. Mesozoic–Cenozoic evolution of the Xining–Minhe and Dangchang basins, northeastern Tibetan Plateau: magnetostratigraphic and biostratigraphic results. *J. Geophys. Res.* **109**, B04402 (2004).
- Fang, X. M. et al. Cenozoic magnetostratigraphy of the Xining Basin, NE Tibetan Plateau, and its constraints on paleontological, sedimentological and tectonomorphological evolution. *Earth-Sci. Rev.* **190**, 460–485 (2019).
- Wang, W. T. et al. Pulsed growth of the West Qinling at ~30 Ma in northeastern Tibet: evidence from Lanzhou Basin magnetostratigraphy and provenance. *J. Geophys. Res.* **121**, 7754–7774 (2016).
- Yue, L. P. et al. Magnetostratigraphy and paleoenvironmental record of Tertiary deposits of Lanzhou Basin. *Chin. Sci. Bull.* **46**, 770–773 (2001).
- Zhang, P. et al. Magnetostratigraphy of the Oligocene mammalian faunas in the Lanzhou Basin, Northwest China. *J. Asian Earth Sci.* **159**, 24–33 (2018).
- Zhang, P., Ao, H., Dekkers, M. J., Li, Y. X. & An, Z. S. Late Oligocene–Early Miocene magnetostratigraphy of the mammalian faunas in the Lanzhou Basin—environmental changes in the NE margin of the Tibetan Plateau. *Sci. Rep.* **6**, 38023 (2016).

39. Licht, A. et al. Resilience of the Asian atmospheric circulation shown by Paleogene dust provenance. *Nat. Commun.* **7**, 12390 (2016).
40. Dai, S. et al. Magnetostratigraphy of Cenozoic sediments from the Xining Basin: tectonic implications for the northeastern Tibetan Plateau. *J. Geophys. Res.* **111**, B11102 (2006).
41. Vandenberghe, N., Hilgen, F. J. & Speijer, R. P. In *The Geologic Time Scale*. (eds Gradstein, F. M., Ogg, J. G., Schmitz, M. & Ogg, G.) 855–922 (Elsevier, Amsterdam, 2012).
42. Pike, C. R., Roberts, A. P. & Verosub, K. L. First-order reversal curve diagrams and thermal relaxation effects in magnetic particles. *Geophys. J. Int.* **145**, 721–730 (2001).
43. Laskar, J., Fienga, A., Gastineau, M. & Manche, H. La2010: a new orbital solution for the long-term motion of the Earth. *Astron. Astrophys.* **532**, A89 (2011).
44. Nesbitt, H. W. & Young, G. M. Early Proterozoic climates and plate motions inferred from major element chemistry of lutite. *Nature* **299**, 715–717 (1982).
45. Wei, G., Li, X. H., Liu, Y., Shao, L. & Liang, X. R. Geochemical record of chemical weathering and monsoon climate change since the early Miocene in the South China Sea. *Paleoceanography* **21**, PA4214 (2006).
46. Luterbacher, H. P. et al. In *A Geologic Time Scale 2004* (eds Gradstein, F. M., Ogg, J. G. & Smith, A. G.) 384–408 (Cambridge University Press, Cambridge, 2004).
47. Westerhold, T. et al. Orbitally tuned timescale and astronomical forcing in the middle Eocene to early Oligocene. *Clim. Past* **10**, 955–973 (2014).
48. Su, Q. D. et al. Detection of strong precession cycles from the late Pliocene sedimentary records of northeastern Tibetan Plateau. *Geochem. Geophys. Geosyst.* <https://doi.org/10.1029/2019GC008447> (2019).
49. White, D. S. & Miller, M. F. Benthic invertebrate activity in lakes: linking present and historical bioturbation patterns. *Aquat. Biol.* **2**, 269–277 (2008).
50. Orme, L. C. et al. Investigating the maximum resolution of mu XRF core scanners: a 1800 year storminess reconstruction from the Outer Hebrides, Scotland, UK. *Holocene* **26**, 235–247 (2016).
51. Nie, J. S. et al. Dominant 100,000-year precipitation cyclicity in a late Miocene lake from northeast Tibet. *Sci. Adv.* **3**, e1600762 (2017).
52. Zachos, J. C., Quinn, T. M. & Salamy, K. A. High-resolution (10⁴ years) deep-sea foraminiferal stable isotope records of the Eocene–Oligocene climate transition. *Paleoceanography* **11**, 251–266 (1996).
53. Tremblin, M., Hermoso, M. & Minoletti, F. Equatorial heat accumulation as a long-term trigger of permanent Antarctic ice sheets during the Cenozoic. *Proc. Natl Acad. Sci. USA* **113**, 11782–11787 (2016).
54. Pagani, M. et al. The role of carbon dioxide during the onset of Antarctic glaciation. *Science* **334**, 1261–1264 (2011).
55. Zhang, Y. G., Pagani, M., Liu, Z. H., Bohaty, S. M. & DeConto, R. A 40-million-year history of atmospheric CO₂. *Philos. Trans. R. Soc. Lond. A* **371**, 10.1098/Rsta.202013.0096 (2013).
56. Pearson, P. N., Foster, G. L. & Wade, B. S. Atmospheric carbon dioxide through the Eocene–Oligocene climate transition. *Nature* **461**, 1110–1114 (2009).
57. DeConto, R. M. & Pollard, D. Rapid Cenozoic glaciation of Antarctica induced by declining atmospheric CO₂. *Nature* **421**, 245–249 (2003).
58. DeConto, R. M. et al. Thresholds for Cenozoic bipolar glaciation. *Nature* **455**, 652–657 (2008).
59. Katz, M. E. et al. Impact of Antarctic circumpolar current development on late Paleogene ocean structure. *Science* **332**, 1076–1079 (2011).
60. Li, J. X. et al. Global cooling and enhanced Eocene Asian mid-latitude interior aridity. *Nat. Commun.* **9**, 3026 (2018).
61. Ramstein, G., Fluteau, F., Besse, J. & Jousseaume, S. Effect of orogeny, plate motion and land sea distribution on Eurasian climate change over the past 30 million years. *Nature* **386**, 788–795 (1997).
62. Bougeois, L. et al. Asian monsoons and aridification response to Paleogene sea retreat and Neogene westerly shielding indicated by seasonality in Paratethys oysters. *Earth Planet. Sci. Lett.* **485**, 99–110 (2018).
63. Zijderveld, J. D. A. In *Methods in Paleomagnetism* (eds Collinson, D. W., Creer, K. M. & Runcorn, S. K.) 254–286 (Elsevier, Amsterdam, 1967).
64. Kirschvink, J. L. The least-squares line and plane and the analysis of palaeomagnetic data. *Geophys. J. R. Astron. Soc.* **62**, 699–718 (1980).
65. Jones, C. H. User-driven integrated software lives: “Paleomag” paleomagnetism analysis on the Macintosh. *Comput. Geosci.* **28**, 1145–1151 (2002).
66. Heslop, D. & Roberts, A. P. Estimation and propagation of uncertainties associated with paleomagnetic directions. *J. Geophys. Res.* **121**, 2274–2289 (2016).
67. Cande, S. C. & Kent, D. V. A new geomagnetic polarity time scale for the Late Cretaceous and Cenozoic. *J. Geophys. Res.* **97**, 13917–13951 (1992).
68. Harrison, R. J. & Feinberg, J. M. FORCinel: an improved algorithm for calculating first-order reversal curve distributions using locally weighted regression smoothing. *Geochem. Geophys. Geosy.* **9**, Q05016 (2008).
69. Blanco, A. et al. Characterization of African dust over southern Italy. *Atmos. Chem. Phys.* **3**, 2147–2159 (2003).
70. Liu, H. J. et al. Magnetic signatures of natural and anthropogenic sources of urban dust aerosol. *Atmos. Chem. Phys.* **19**, 731–745 (2019).
71. Yu, Z. W. & Ding, Z. L. An automatic orbital tuning method for paleoclimate records. *Geo. Res. Lett.* **25**, 4525–4528 (1998).
72. Mann, M. E. & Lees, J. M. Robust estimation of background noise and signal detection in climatic time series. *Clim. Change* **33**, 409–445 (1996).
73. Li, M. S., Hinnov, L. & Kump, L. Acycle: time-series analysis software for paleoclimate research and education. *Comput. Geosci.* **127**, 12–22 (2019).

Acknowledgements

This study was supported financially by the Chinese Academy of Sciences (CAS) Strategic Priority Research Program (XDB 40000000), the Second Tibetan Plateau Scientific Expedition and Research (STEP) program (2019QZKK0707, 2019QZKK0101), the CAS Key Research Program of Frontier Sciences (QYZDB-SSW-DQC021), the National Natural Science Foundation of China, the Ministry of Science and Technology of China, Australian Research Council (ARC) Australian Laureate Fellowship grant FL120100050 to E.J.R., ARC grant DP120103952 to A.P.R., ERC consolidator grant MAGIC 649081 to G.D.-N., N.B., N.M., and A.L., and the Bolin Center for Climate Research to H.C.

Author contributions

H.A., G.D.-N., and Z.S.A. conceived the idea of this study and participated in the fieldwork. E.J.R., A.P.R., A.L., Q.S.L., Z.H.L., and M.J.D. contributed to data analysis, interpretation, and discussion. H.A. and P.Z. performed the magnetic, mineralogical, and multi-proxy measurements. J.-B.L. and C.J.P. contributed to the establishment of related climatic dynamics. Z.H.L., H.K.C., and G.Q.X. helped with marine palaeoclimatic interpretation. Z.D.J., X.K.Q., N.B., N.M., J.Y., and Q.S. helped with terrestrial palaeoclimatic interpretation. C.J.H. helped with the orbital tuning and spectral analysis. H.A., G.D.-N., and Z.S.A. led the manuscript writing with intellectual contributions from all coauthors.

Competing interests

The authors declare no competing interests.

Additional information

Supplementary information is available for this paper at <https://doi.org/10.1038/s41467-020-18824-8>.

Correspondence and requests for materials should be addressed to H.A., G.D.-N. or Z.A.

Peer review information *Nature Communications* thanks Erwin Appel, Peter Lippert and the other, anonymous, reviewer(s) for their contribution to the peer review of this work. Peer reviewer reports are available.

Reprints and permission information is available at <http://www.nature.com/reprints>

Publisher's note Springer Nature remains neutral with regard to jurisdictional claims in published maps and institutional affiliations.



Open Access This article is licensed under a Creative Commons Attribution 4.0 International License, which permits use, sharing, adaptation, distribution and reproduction in any medium or format, as long as you give appropriate credit to the original author(s) and the source, provide a link to the Creative Commons license, and indicate if changes were made. The images or other third party material in this article are included in the article's Creative Commons license, unless indicated otherwise in a credit line to the material. If material is not included in the article's Creative Commons license and your intended use is not permitted by statutory regulation or exceeds the permitted use, you will need to obtain permission directly from the copyright holder. To view a copy of this license, visit <http://creativecommons.org/licenses/by/4.0/>.

© The Author(s) 2020